

Influence of incomplete fusion in $^{12}\text{C}+^{193}\text{Ir}$ at $E_{lab} = 64\text{--}84$ MeV

Amanjot^{1,*}, Priyanka¹, Rupinderjeet Kaur¹, Subham Kumar¹, Malika Kaushik^{1,†}, Manoj Kumar Sharma², Yashraj Jangid³, Rakesh Kumar^{3,‡} and Pushpendra P. Singh^{1,§}
¹*Department of Physics, Indian Institute of Technology Ropar, Rupnagar - 140 001, Punjab, India*
²*Department of Physics, University of Lucknow, Lucknow - 226 007, Uttar Pradesh, India and*
³*Inter-University Accelerator Centre, New Delhi - 110 067, India*
(Dated: March 4, 2025)

Excitation functions of several evaporation residues populated via complete and/or incomplete fusion in $^{12}\text{C}+^{193}\text{Ir}$ system have been measured at energies $\approx 64\text{--}84$ MeV, and analyzed in the framework of theoretical model code PACE4. The xn channels are found to be predominantly populated via complete fusion; however, some of the pxn channels decay via their precursor. A substantial enhancement has been observed in the case of α -emitting channels over PACE4 calculations, indicating the onset of a reaction mode not incorporated in this code, e.g., incomplete fusion. For better insights into the onset and influence of incomplete fusion, the cross-section data have been analyzed in terms of different entrance-channel parameters. The findings of the present study reinstate the importance of projectile energy, entrance-channel mass-asymmetry, and the Coulomb factor of interacting partners in incomplete fusion dynamics. Further, the impact of projectile break-up on complete fusion has also been discussed in the framework of the Universal Fusion Function. As much as $\approx 12\%$, fusion suppression has been observed potentially due to projectile break-up.

I. INTRODUCTION

Low-energy heavy-ion (HI) induced reactions are crucial for generating novel and intriguing states of nuclei for spectroscopic investigations and facilitating the production of new nuclear species [1–6]. Generally, nuclear reactions below 8 MeV/nucleon predominantly lead to the population of (i) complete (CF) and (ii) incomplete fusion (ICF) residues. In the case of CF, for driving input angular momentum $\ell < \ell_{crit}$, the projectile completely coalesces with the target nucleus, forming an excited compound nucleus (CN) involving all nucleonic degrees of freedom of the interacting partners [7, 8]. However, the ICF occurs for relatively higher ℓ -values, i.e., $\ell > \ell_{crit}$, in which the projectile dissociates into its constituents [9, 10]. One of the fragments fuses with the target nucleus to form an incompletely fused composite system, and the remnant releases in the forward cone, nearly undeflected, with the projectile velocity [11–13]. Peripheral collisions have been reported to create favorable conditions for ICF reactions [14–16]. A series of experiments have been performed using ^{12}C projectile, with ^{103}Rh [17, 18], ^{115}In [19], ^{128}Te [20], ^{159}Tb [21], ^{160}Gd [9], ^{165}Ho [22, 23], ^{169}Tm [24, 25], ^{175}Lu [26], ^{181}Ta [27, 28], ^{197}Au [28, 29], ^{208}Pb [30] targets, in which ICF has been attributed to the low α separation energy, i.e., ~ 7.3 MeV, of ^{12}C projectile into $^8\text{Be}+\alpha$, and/or $\alpha+\alpha+\alpha$ fragment configurations [31].

Several theoretical models, e.g., break-up fusion (BUF) model [32], sum-rule model [10], promptly emitted parti-

cles (PEPs) model [33], etc., are known to elucidate ICF dynamics to some extent at energies > 10 MeV/nucleon, in specific instances. However, the intricacies of ICF at energies as low as 3–5 MeV/nucleon are not yet fully understood. Morgenstern et al. [34] correlated the onset of ICF with entrance-channel mass-asymmetry (μ_m) at energies > 10 MeV/nucleon. However, at low incident energies, in ref. [26, 27, 35, 36], the projectile-dependence of mass-asymmetry (μ_m) systematics has been observed. The influence of projectile structure on ICF in terms of Q_α [22, 37–39], and neutron excess projectile [21, 37, 39] has been realised. Sharma et al. [37], found that $1n$ excess in ^{13}C leads to a reduced ICF fraction due to a higher negative Q_α value than ^{12}C projectile. Rafiei et al. [40] indicated a non-dependence on Z_T , while Hinde et al. [41], and Gomes et al. [42] suggested a near-proportional relationship with Z_T . Shuaib et al. [43] suggested a linear increase in ICF strength with the Coulomb factor ($Z_P Z_T$). However, upon re-examining the relationship between $Z_P Z_T$ and ICF, it has been found that ICF exhibits a linear trend separately for each projectile [22, 26].

Further, the ICF fraction in terms of target deformation has been discussed in refs. [23, 44–46]. Giri et al. [47] indicated that the ICF fraction increases exponentially with deformation parameter (β_2^T), deformation length ($\beta_2^T R^T$), and neutron excess ($N-Z$)^T rather than linear growth, indicating projectile structure dependence of ICF. The additional parameters such as $Z_P Z_T \beta_2^T$, $Z_P Z_T / (1 - \beta_2^T)$ [26], $\beta_2^T \mu_m$, $Z_P Z_T \mu_m$ [48] have been introduced without much explanation of their relation with different entrance-channel parameters. These combined parameters are not suitable for explaining ICF, especially for spherical and deformed targets. Nasirov et al. [49] found that the increased fusion barrier, angular velocity, and decreased excitation energy contribute to the ICF at a large orbital angular momentum. Eudes et al. [50] describe fusion EFs independently in terms of μ_m and

* amanjot.19phz0004@iitrpr.ac.in

† Presently at: National Institute of Technology (NIT) Kurukshetra - 136 119, Kurukshetra, Haryana, India

‡ deceased

§ pps@iitrpr.ac.in

TABLE I. List of identified ERs in $^{12}\text{C}+^{193}\text{Ir}$ system.

Channel	ER	Half-life $t_{1/2}$	Spin J^π	Gamma E_γ (keV)	Intensity I_γ (%)
4n	^{201}Bi	103 m	$9/2^-$	629.1	26.0
5n	^{200}Bi	36.4 m	7^+	462.34	98.0
	$^{200}\text{Bi}^m$	31 m	2^+	1026.49	91.0
p3n	^{201}Pb	9.33 h	$5/2^-$	331.15	77.0
p4n	^{200}Pb	21.5 h	0^+	147.63	38.2
αn	^{200}Tl	26.1 h	2^-	367.94	87.0
$\alpha 2n$	^{199}Tl	7.42 h	$1/2^+$	208.20	12.3
$\alpha 3n$	$^{198}\text{Tl}^g$	5.3 h	2^-	411.8	80.0
$2\alpha n$	$^{196}\text{Au}^m$	9.6 h	12^-	147.81	43.5

isospin. Yadav et al. [51] elucidated the trends of ICF by considering both the total asymmetry and the system parameters. The system parameter appears to provide a more satisfactory explanation of the experimental data, as it encompasses the $Z_P Z_T$ and the masses of the interacting nuclei. Moreover, several studies suggested that ICF can be selectively used to produce high-spin states in the final reaction products compared to the CF [52–54].

In this work, the channel-by-channel EFs of several evaporation residues (ERs) populated via xn , pxn , αxn , and $2\alpha xn$ channels have been measured in $^{12}\text{C}+^{193}\text{Ir}$ system at energies 5–7 MeV/nucleon and analyzed in the framework of statistical model code PACE4.

II. EXPERIMENTAL DETAILS

Experiments were conducted at the Inter-University Accelerator Centre (IUAC), New Delhi, using the stacked-foil activation technique followed by offline γ -spectroscopy. ^{193}Ir targets of thickness 17–60 $\mu\text{g}/\text{cm}^2$ were fabricated on 1–1.5 mg/cm^2 thick Al foil [55]. Al-backed targets were irradiated in the General Purpose Scattering Chamber (GPSC) with $^{12}\text{C}^{6+}$ beams at 81 and 84 MeV, with 1–2 pA beam current, for 6–8 hours. In this case, the Al backing of the target captures the ERs recoiling out of the target foil and degrades the beam energy for subsequent target foils [56]. After irradiation, the stack was taken out from GPSC and counted offline using pre-calibrated high-resolution clover HPGe detectors coupled with a CAMAC-based DAQ system [57, 58]. Standard γ sources (e.g., ^{152}Eu , ^{60}Co , and ^{133}Ba) were used for energy and efficiency calibration.

The ERs have been identified by their characteristic γ -rays and confirmed through the decay curve analysis. Fig. 1(a) shows a portion of the γ -ray spectrum obtained at 84 MeV in which the peaks of different ERs are marked. As a representative case, the decay curve of $^{200}\text{Bi}(5n)$ is given in Fig. 1(b–c) [59]. The same approach has been followed to identify all ERs listed in Table I with their spectroscopic properties. The production cross-sections (σ_{exp}) of ERs have been calculated using

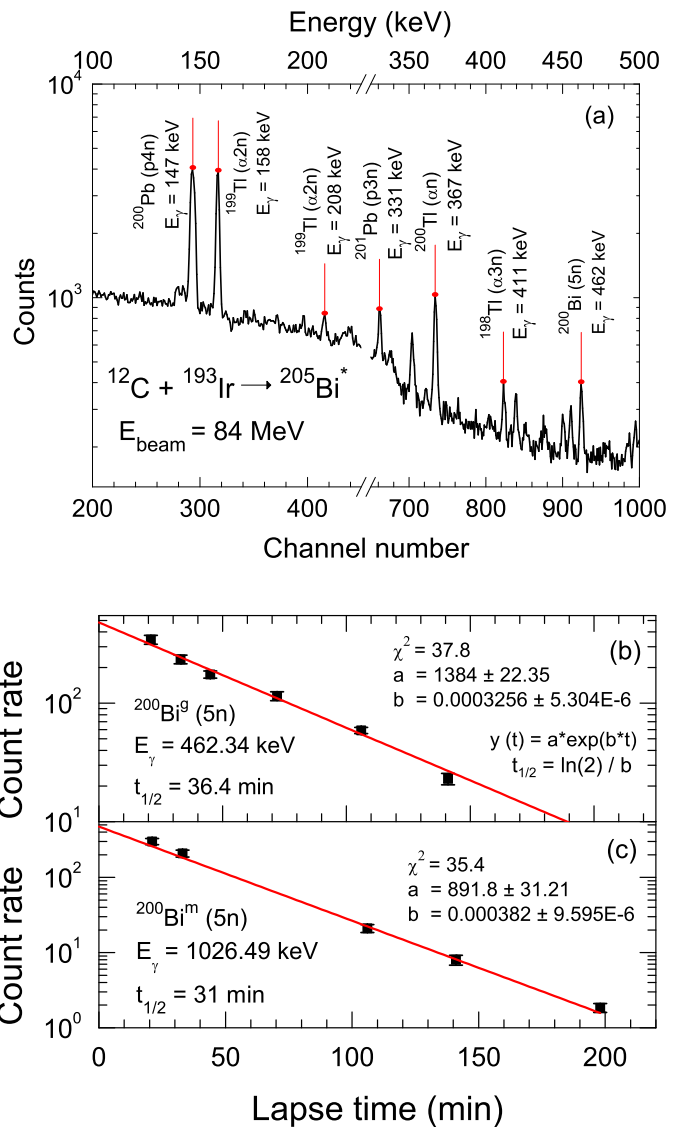


FIG. 1. (a) A portion of γ -ray spectrum obtained at 84 MeV for $^{12}\text{C}+^{193}\text{Ir}$ system, (b) the decay curve for ground state of ^{200}Bi nuclei reproducing a half-life of 36.4 min by following $E_\gamma=462.34 \text{ keV}$, and (c) the decay curve for metastable state of ^{200}Bi displaying a half-life of 31 min by following $E_\gamma=1026.49 \text{ keV}$.

a standard formulation [60] and listed in Tables II and III. The overall error in σ_{exp} is estimated to be $\leq 13\%$, excluding the uncertainties in nuclear data, which have been taken from the Table of Isotopes [61] and Nuclear Wallet Card [62].

III. RESULTS AND ANALYSIS

Experimentally measured cross-sections (σ_{exp}) of ERs, with overall errors, have been plotted against projectile energy to generate channel-by-channel EFs and analyzed using the statistical model code PACE4 [63]. In this code,

TABLE II. Experimental cross sections (σ_{exp}) of ERs populated in the $^{12}\text{C}+^{193}\text{Ir}$ system via CF process.

E_{lab} (MeV)	^{201}Bi ($4n$) σ (mb)	$^{200}\text{Bi}^{g+m}$ ($5n$) σ (mb)	^{201}Pb ($p3n$) σ (mb)	^{200}Pb ($p4n$) σ (mb)
83.99	26.00 ± 6.64	626.35 ± 65.55	9.39 ± 3.12	83.80 ± 24.58
80.99	69.85 ± 16.81	693.17 ± 83.04	17.58 ± 5.49	67.05 ± 20.12
79.36	96.68 ± 15.56	662.90 ± 68.77	22.61 ± 5.37	56.70 ± 14.48
76.53	176.11 ± 23.24	562.15 ± 77.79	29.83 ± 6.59	32.02 ± 8.17
74.82	250.95 ± 32.95	405.72 ± 47.82	32.47 ± 7.41	21.37 ± 7.17
71.86	389.82 ± 40.53	182.48 ± 20.62	34.03 ± 7.36	7.42 ± 2.24
70.06	401.05 ± 56.12	99.66 ± 14.38	29.88 ± 6.57	2.68 ± 0.72
64.37	253.16 ± 25.55	28.35 ± 5.63	6.84 ± 1.48	1.21 ± 0.51

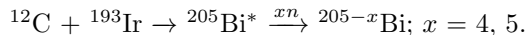
TABLE III. Experimental cross-sections (σ_{exp}) of ERs populated in the $^{12}\text{C}+^{193}\text{Ir}$ system via CF and/or ICF processes.

E_{lab} (MeV)	^{200}Tl (αn) σ (mb)	^{199}Tl ($\alpha 2n$) σ (mb)	$^{198}\text{Tl}^g$ ($\alpha 3n$) σ (mb)	$^{196}\text{Au}^m$ ($2\alpha n$) σ (mb)
83.99	50.01 ± 9.35	26.32 ± 6.16	18.48 ± 2.20	125.47 ± 20.21
80.99	112.26 ± 24.71	22.82 ± 6.58	33.45 ± 3.95	73.49 ± 14.0
79.36	80.04 ± 13.29	22.31 ± 5.41	33.58 ± 3.90	83.60 ± 13.32
76.53	52.87 ± 15.94	29.88 ± 5.08	43.68 ± 5.16	70.49 ± 9.83
74.82	28.93 ± 5.56	27.77 ± 3.39	46.83 ± 4.87	78.10 ± 13.83
71.86	35.04 ± 7.23	27.74 ± 4.54	38.92 ± 5.54	41.62 ± 6.16
70.06	33.75 ± 7.47	28.56 ± 4.87	31.00 ± 4.02	20.68 ± 3.67
64.37	11.38 ± 2.82	20.86 ± 4.80	10.75 ± 1.36	8.29 ± 1.55

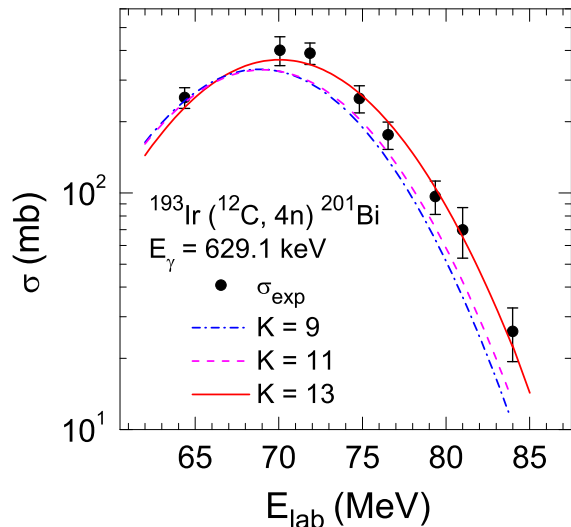
the level density parameter, $a = A/K \text{ MeV}^{-1}$, is crucial, where A is the mass number of CN, and K is a free parameter that may be adjusted to reproduce experimental EFs. Since the code PACE4 takes only CF into account, any discrepancies between experimental cross-sections and PACE4 predictions may indicate contributions from ICF in α -emitting channels and/or pre-equilibrium emission processes, especially for neutron-emitting channels at higher energies [64]. Detailed channel-by-channel analysis of EFs using PACE4 is provided in the following sections.

A. xn - channels

In CF channels, ^{12}C may completely fuse with ^{193}Ir nuclei to form an excited CN, $^{205}\text{Bi}^*$, which may eventually decay via several neutrons and γ -rays. For example, the ERs ^{201}Bi and ^{200}Bi may be populated as,



For an insight into how well the production of these residues can be explained by the formation and decay of CN, the EF of $^{201}\text{Bi}(4n)$ is compared with PACE4 using $K = 9, 11, 13$ in Fig. 2. As can be seen from this figure, the cross-sections of $4n$ channel are reasonably reproduced by PACE4 using $a = A/13 \text{ MeV}^{-1}$ within the experimental uncertainties, indicating the population of ^{201}Bi only via CF. Therefore, $K = 13$ can be used as an optimized parameter for analyzing other ERs formed in this system at the studied energy range.

FIG. 2. Experimental EF of $^{201}\text{Bi}(4n)$ compared with PACE4 calculations using different values of $K = 9, 11,$ and 13 .

The EF of $^{200}\text{Bi}(5n)$ is plotted in Fig. 3(a) with PACE4 calculations. As can be seen from this figure, the PACE4 calculations over-predict the cross-section of ^{200}Bi , indicating the missing contribution at all energies. In further analysis, it has been found that ^{200}Bi is populated via both metastable and ground states. Therefore, the cross-sections of metastable and ground states have been measured individually and plotted in Fig. 3(b) along with the

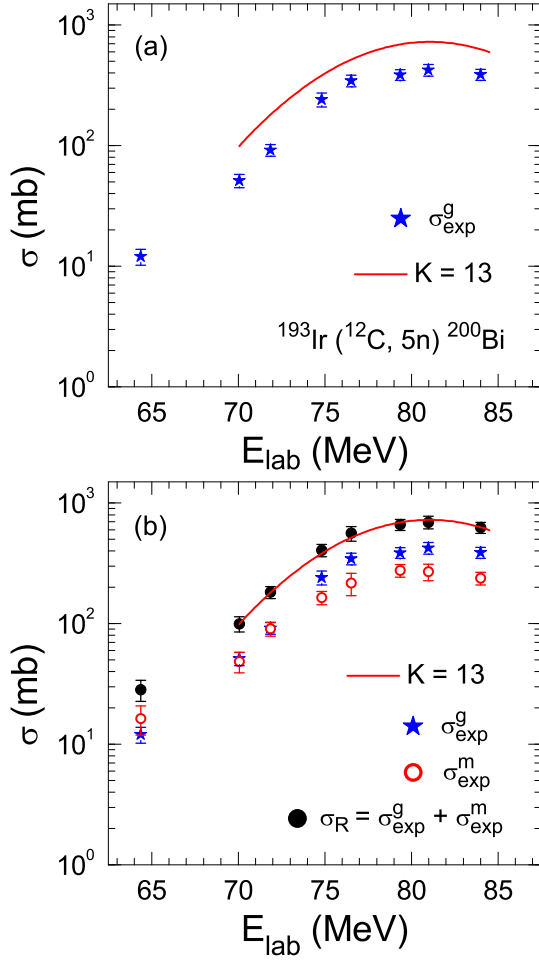


FIG. 3. The EF of $^{200}\text{Bi}(5n)$ for (a) ground state, and (b) ground and metastable states along with σ_R is compared with PACE4 using $K = 13$.

sum of both states, i.e., $\sigma_R = \sigma_{exp}^g + \sigma_{exp}^m$. The PACE4 reproduces the experimental EFs fairly well in this figure, except at ≈ 64 MeV. Based on results presented in Fig. 2 and 3(b), it can be inferred that the residues ^{201}Bi and ^{200}Bi are populated via emission of $4n$ and $5n$ channels, respectively, from a fully equilibrated CN $^{205}\text{Bi}^*$ formed via CF in $^{12}\text{C} + ^{193}\text{Ir}$ reaction.

B. pxn - channels

Fig. 4(a) shows the EF of ^{201}Pb (half-life = 9.33 h) populated via $p3n$ channel. As can be noticed from this figure, PACE4 substantially under-predicts the EF, indicating the presence of its higher charge precursor, ^{201}Bi , through β^+ emission and/or electron capture (EC). The population of ^{201}Pb through different routes may be explained as,

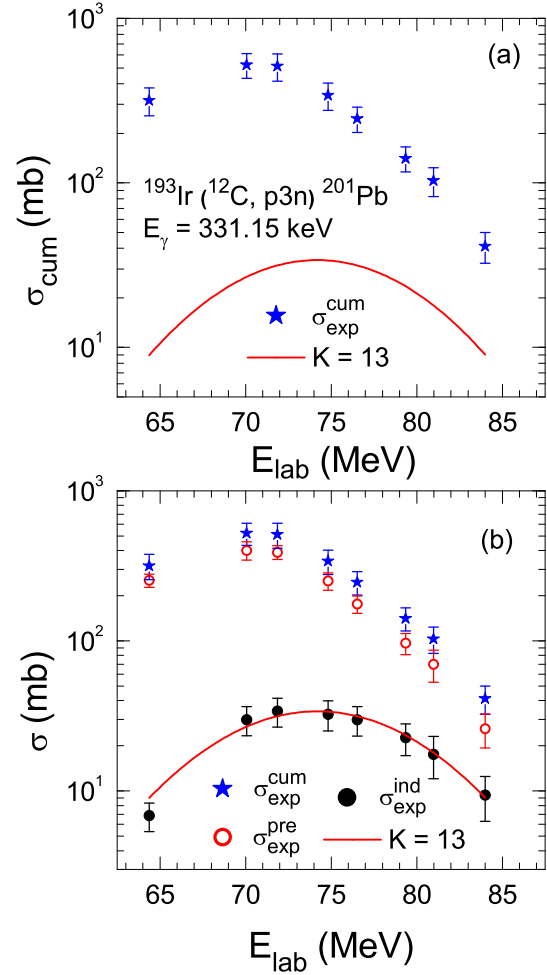
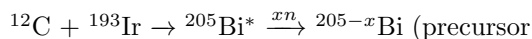


FIG. 4. (a) The experimental EF of ^{201}Pb ($p3n$) residue, (b) σ_{exp}^{cum} , σ_{exp}^{pre} and σ_{exp}^{ind} contributions are compared with PACE4 calculations for $K = 13$.

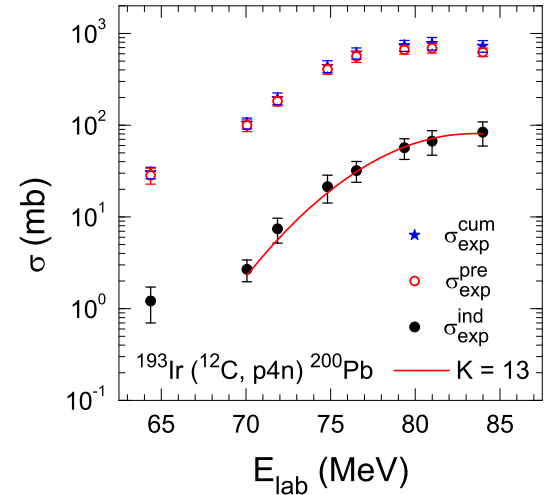
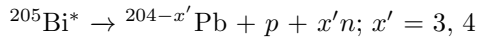


FIG. 5. Experimental EF of $^{200}\text{Pb}(p4n)$ residue. The contributions of σ_{exp}^{pre} and σ_{exp}^{ind} are plotted with σ_{exp}^{cum} and PACE4 calculations for $K = 13$.

nucleus); $x = 4, 5$



$^{205-x}\text{Bi} \xrightarrow{\beta^+/EC} ^{204-x'}\text{Pb}$ (daughter nucleus);
 $x = 4, 5$ and $x' = 3, 4$, provided, $t_{1/2}^p \ll t_{1/2}^d$.

In Fig. 4(b), the independent contribution of ^{201}Pb obtained using successive radioactive decay formulation proposed by Cavinato et al. [65] is presented. In this figure, the independent cross-section of $^{201}\text{Pb}(p3n)$ is reproduced reasonably well by PACE4 for $K = 13$ after subtracting the contribution of ^{201}Bi from the cumulative cross-section.

Similarly, the $^{200}\text{Pb}(p4n)$ residue (half-life = 21.5 h) is fed from its higher charge isobar, $^{200}\text{Bi}(5n)$, through β^+ and/or EC decay. In Fig. 5, the value of σ_{exp}^{ind} for $^{200}\text{Pb}(p4n)$ residue is compared with PACE4 along with σ_{exp}^{pre} and σ_{exp}^{cum} . As shown in this figure, the value of σ_{exp}^{ind} is in good agreement with the PACE4 for $a = A/13$ MeV^{-1} . Based on the results presented in Fig. 4(b) and 5, it can be inferred that the ^{201}Pb and ^{200}Pb are populated via CF of ^{12}C with ^{193}Ir .

1. Remark on the accuracy of CF cross-sections

Fig. 6(a) shows the comparison of the sum of experimental cross-sections of xn and pxn channels ($\Sigma\sigma_{exp}^{xn+pxn}$) with PACE4. As can be seen from this figure, the values of $\Sigma\sigma_{exp}^{xn+pxn}$ at different energies are in good agreement with PACE4 calculations, indicating the production of these residues via de-excitation of fully equilibrated CN formed in a CF reaction. Thus, the level density parameter $a = A/13$ MeV^{-1} can analyze other channels in the measured energy range.

To further supplement the discussion, an attempt has been made to deduce the Coulomb barrier (V_b) for $^{12}\text{C}+^{193}\text{Ir}$ system by analyzing the experimental CF cross-sections, σ_{CF} [10] as,

$$\sigma_{CF} = \pi R^2 \left(1 - \frac{V_b}{E_{c.m.}}\right), \quad (1)$$

where V_b is the Coulomb barrier, $E_{c.m.}$ is center-of-mass energy, and R is the interaction radius.

The value of σ_{CF} is plotted as a function of $1/E_{c.m.}$ in Fig. 6(b). The fitting of the data results in a straight line that intersects the x-axis at the inverse of beam energy equivalent to V_b , i.e., 56.17 MeV, in the center-of-mass frame. The value of V_b deduced using this analysis reproduces the calculated one, thereby bolstering the accuracy of the present measurements.

C. αxn - channels

The EFs of $^{200}\text{Tl}(\alpha n)$ and $^{199}\text{Tl}(\alpha 2n)$ channels in Fig. 7(a)-(b) show a significant enhancement compared

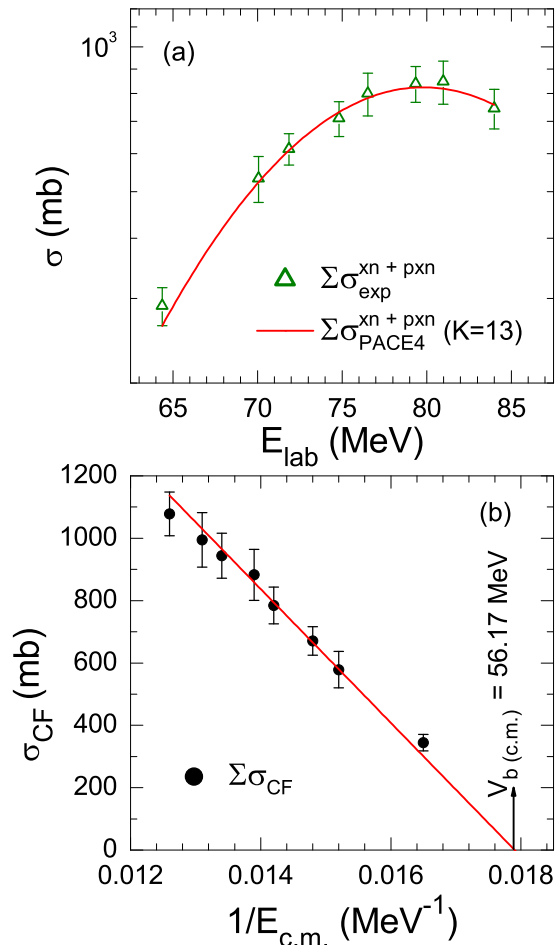


FIG. 6. (a) The sum of the experimental cross-sections of xn and pxn channels ($\Sigma\sigma_{exp}^{xn+pxn}$) compared with PACE4 ($\Sigma\sigma_{PACE4}^{xn+pxn}$). (b) CF cross-sections plotted with the inverse of $E_{c.m.}$. The solid line represents the best fit to the data points.

to PACE4 calculations. A similar trend has been observed for $^{198}\text{Tl}(\alpha 3n)$ in Fig. 8(a). It may be pointed out that the α -emitting channels may originate from both CF and/or ICF. For example, $^{198}\text{Tl}(\alpha 3n)$ may be populated via (i) CF of ^{12}C with ^{193}Ir after emission of an α particle and 3 neutrons from $^{205}\text{Bi}^*$, or via (ii) ICF where ^8Be may fuse with ^{193}Ir forming an incompletely fused composite (IFC) system $^{201}\text{Tl}^*$, with remnant α -particle emitted in the forward cone. The IFC $^{201}\text{Tl}^*$ may decay via $3n$ leading to the population of ^{198}Tl . Both the processes may be represented as,

1. CF of ^{12}C with ^{193}Ir :
 $^{12}\text{C} + ^{193}\text{Ir} \rightarrow ^{205}\text{Bi}^* \rightarrow ^{201-x}\text{Tl} + \alpha xn; (x = 3)$
2. ICF of ^{12}C with ^{193}Ir :
 $^{12}\text{C} (^8\text{Be} + \alpha) \rightarrow ^8\text{Be} + ^{193}\text{Ir} \rightarrow ^{201}\text{Tl}^*$
 $^{201}\text{Tl}^* \rightarrow ^{201-x}\text{Tl} + xn + \alpha$; where α particle is a spectator, and $x = 3$.

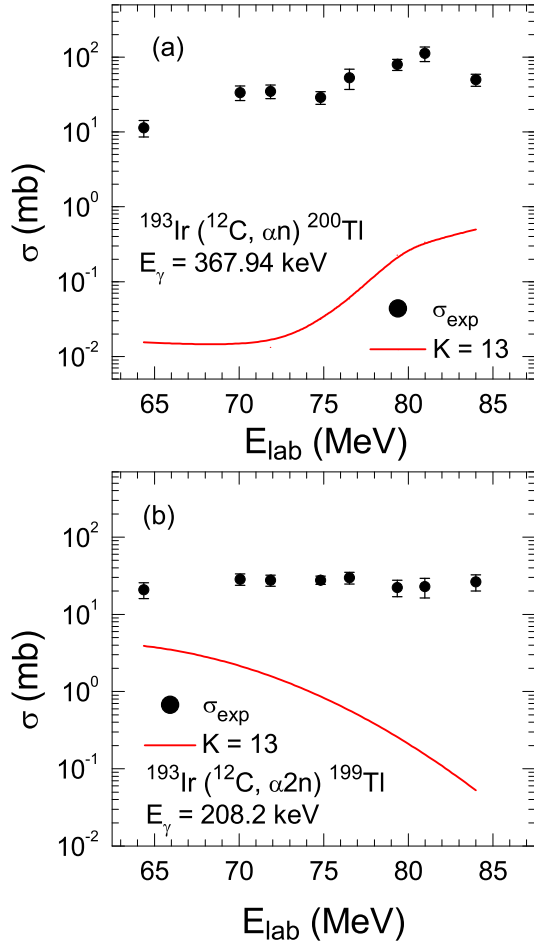


FIG. 7. Experimental EFs of (a) $^{200}\text{Tl}(\alpha n)$, and (b) $^{199}\text{Tl}(\alpha 2n)$ expected to be populated via CF and/or ICF of ^{12}C with ^{193}Ir .

Further, the EF of $^{198}\text{Tl}(\alpha 3n)$ residue is plotted in Fig. 8(a) with PACE4 calculations. As seen from this figure, the experimental cross-sections are enhanced over the theoretical calculations, hinting towards the contribution of ICF. Similar enhancement is observed in case of $^{196}\text{Au}^m(2\alpha n)$ plotted in Fig. 8(b).

For better insight into the onset of α -emitting channels, the sum of experimental EFs of α -emitting channels, $\Sigma\sigma_{exp}^{\alpha xn+2\alpha n}$, is compared with PACE4 ($\Sigma\sigma_{PACE4}^{\alpha xn+2\alpha n}$) calculations in Fig. 9. The EFs of α -emitting channels have been calculated using the same input parameters to reproduce the EFs of xn/pxn channels. As illustrated in Fig. 9, the sum of experimentally measured α -emitting channels is substantially higher than that calculated using PACE4, which may be attributed to the ICF fraction as the code PACE4 takes only CF into account.

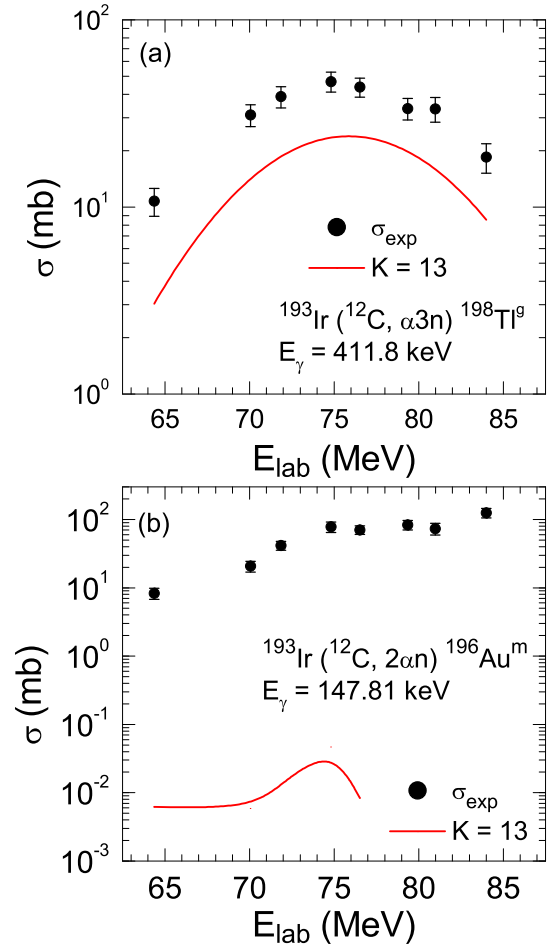


FIG. 8. Experimental EFs of (a) $^{198}\text{Tl}(\alpha 3n)$ in the ground state, and (b) $^{196}\text{Au}^m(2\alpha n)$ populated in the metastable state compared with PACE4 calculations.

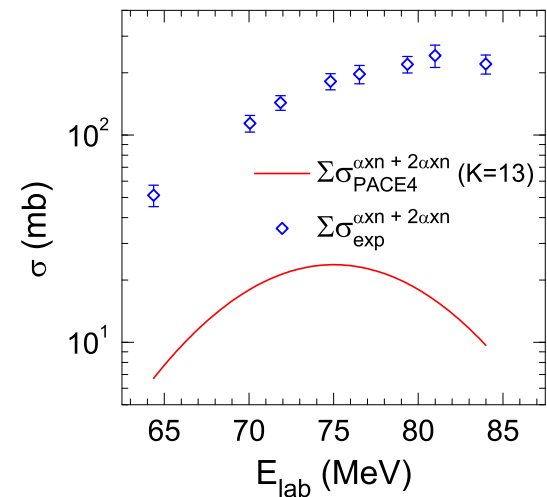


FIG. 9. Experimental EFs of all α -emitting channels ($\Sigma\sigma_{exp}^{\alpha xn+2\alpha n}$) identified in $^{12}\text{C}+^{193}\text{Ir}$ system compared with PACE4 ($\Sigma\sigma_{PACE4}^{\alpha xn+2\alpha n}$) calculations.

1. Influence of α -emitting channels

To visualize the influence of ICF in α -emitting channels, total fusion cross-section (σ_{TF}) is plotted in Fig. 10(a) along with σ_{CF} and σ_{ICF} . It is important to mention that the activation technique has limitations, with channels having shorter half-lives. Therefore, the σ_{CF} value has been corrected by including corresponding unmeasured PACE4 values in CF channels. However, in the evaluation of σ_{ICF} , no correction has been made to incorporate the unmeasured ICF channels. As can be seen from this figure, the gap between σ_{TF} and σ_{CF} seems to be widened with increasing projectile energy. In order to understand how ICF competes with CF, the percentage fraction of ICF, F_{ICF} , has been deduced using the data presented in Fig. 10(a) and plotted against $E_{c.m.}/V_b$ in Fig. 10(b). This figure shows that the value of F_{ICF} increases from $\approx 12\%$ to $\approx 18\%$. This trend suggests that the break-up probability of ^{12}C increases with incident energy, likely due to input angular momentum at higher energies, which flattens the fusion pocket in the effective potential. As a result, the projectile breaks up into α -clusters to restore the fusion pocket and sustain angular momentum.

IV. EFFECT OF ENTRANCE-CHANNEL PARAMETERS ON ICF

The value of F_{ICF} for various projectile-target combinations has been analyzed in terms of mass-asymmetry and Coulomb factor to understand how entrance-channel parameters affect the onset of ICF.

A. Mass-asymmetry (μ_m)

Entrance-channel mass-asymmetry ($\mu_m = \frac{A_T - A_P}{A_T + A_P}$) dependence of ICF has been investigated for different projectile-target combinations. As proposed by Morgenstern et al.[34], the systems with higher μ_m contribute significantly to ICF at the same relative velocity, $v_{rel} = [\frac{2(E_{c.m.} - V_b)}{\mu}]^{1/2}$, where μ is the reduced mass of the system in u , which is converted to MeV/c^2 . The value of F_{ICF} for $^{12}\text{C} + ^{193}\text{Ir}$ system has been compared with reactions involving projectiles ^{12}C , ^{13}C , ^{16}O and ^{18}O with various targets displayed in Table IV at a constant $v_{rel} = 0.053c$ in Fig. 11. The results show a linear increase in F_{ICF} with entrance-channel μ_m for each projectile (^{12}C , ^{13}C , ^{16}O , and ^{18}O). Further, ^{16}O -induced reactions have higher F_{ICF} values as compared to ^{12}C with the same targets, indicating strong projectile dependence within the mass-asymmetry systematics [35]. Based on data presented in Fig. 11, it can be inferred that the ICF fraction depends on the projectile structure at the studied energy range.

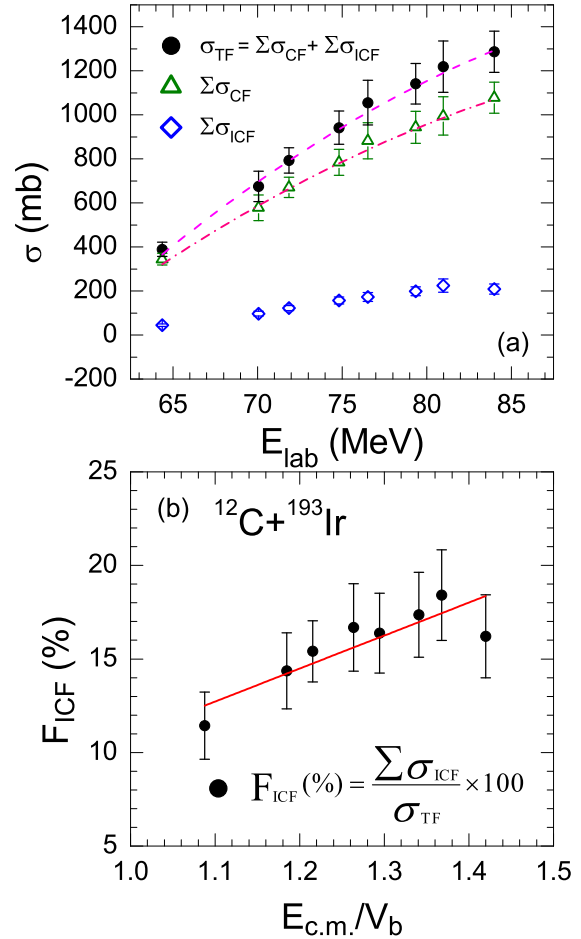


FIG. 10. (a) The value of σ_{TF} along with the σ_{CF} and σ_{ICF} as a function of incident energy, (b) F_{ICF} as a function of $E_{c.m.}/V_b$.

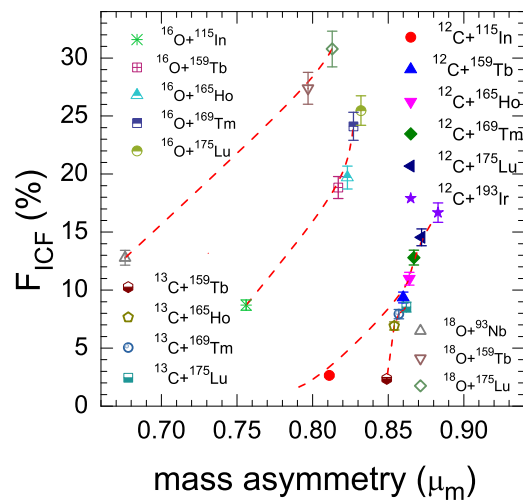


FIG. 11. F_{ICF} at $v_{rel} = 0.053c$ for various α and non- α -cluster projectiles with different targets as a function of μ_m .

TABLE IV. The mass-asymmetry, Coulomb factor, neutron skin thickness, and F_{ICF} of ^{12}C , ^{13}C , ^{16}O and ^{18}O induced reactions with different targets at a constant relative velocity ($v_{rel} = 0.053c$).

System	μ_m	$Z_P Z_T$	F_{ICF} (%)	Ref.
Projectile: ^{12}C				
^{115}In	0.811	294	2.645	[19]
^{159}Tb	0.860	390	9.36	[66]
^{165}Ho	0.864	402	10.98	[67]
^{169}Tm	0.867	414	12.80	[25]
^{175}Lu	0.872	426	14.55	[26]
^{193}Ir	0.883	462	17.13	Present work
Projectile: ^{13}C				
^{159}Tb	0.849	390	2.35	[66]
^{165}Ho	0.854	402	6.12	[22]
^{169}Tm	0.857	414	7.93	[68]
^{175}Lu	0.862	426	8.54	[26]
Projectile: ^{16}O				
^{115}In	0.756	392	8.71	[69]
^{159}Tb	0.817	520	18.84	[70]
^{165}Ho	0.823	536	19.70	[71]
^{169}Tm	0.827	552	24.11	[35]
^{175}Lu	0.832	568	25.47	[72]
Projectile: ^{18}O				
^{93}Nb	0.676	328	12.78	[39]
^{159}Tb	0.797	520	27.39	[73]
^{175}Lu	0.813	568	30.78	[72]

B. Coulomb factor ($Z_P Z_T$)

Fig. 12 displays the ICF strength function in terms of Coulomb factor ($Z_P Z_T$) spanning a range of ≈ 294 –568 for the systems presented in Fig. 11. As seen in this figure, the value of F_{ICF} increases linearly with $Z_P Z_T$, indicating a strong influence of the Coulomb force field. As the projectile approaches the target nucleus, the impact of the Coulombic interaction intensifies, thereby increasing the likelihood of projectile break-up, followed by the fusion of one or more constituent fragments with the target nuclei. The α -cluster structure projectiles (e.g., ^{12}C , ^{16}O) exhibit increasing ICF fraction trends and align on the same line, suggesting consistency in their behavior. However, non- α -cluster projectiles (^{13}C and ^{18}O) also show increasing trends in ICF, but separately for each projectile, contrary to recent findings [43].

From data presented in Fig. 12, it may be concluded that the structural characteristics of the projectile exert a substantial influence on ICF. However, it is insufficient in explaining ICF dynamics for systems with identical $Z_P Z_T$ values displayed in Table IV. Despite similar $Z_P Z_T$, systems exhibit varying ICF contributions, not solely explained by the Coulomb factor.

C. Projectile structure dependence of ICF

As can be seen from Fig. 11 and Fig. 12, the ICF fraction for ^{13}C projectile with various targets seems to be lesser than ^{12}C projectile with the same targets. The

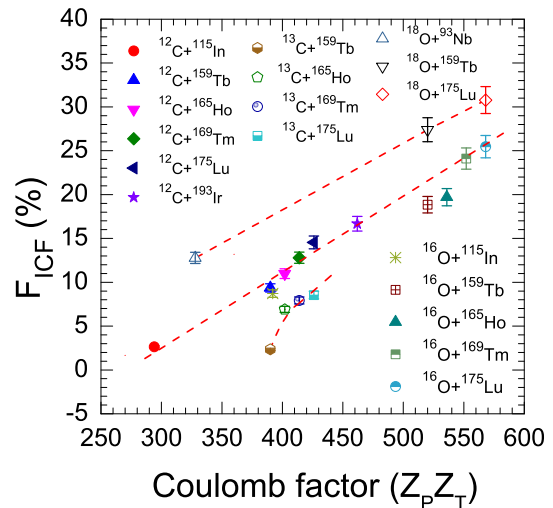


FIG. 12. F_{ICF} for various systems at a constant $v_{rel} = 0.053c$ as a function of $Z_P Z_T$.

^{13}C projectile having one excess neutron results in rather weak binding forces as compared to ^{12}C , thus ^{13}C projectile has a larger probability of break-up. Following the neutron excess in the projectile ^{13}C , the contribution of ICF is expected to be more in the case of ^{13}C projectile as compared to the ^{12}C projectile. However, the ^{13}C projectile exhibits a lower probability of ICF for the same targets. To understand this difference, it is crucial to consider the characteristics of the projectile nucleus.

This study analyzes the probability of ICF as a function of the projectile Q_α value. Projectile Q_α values (-7.37 MeV for ^{12}C , -10.65 MeV for ^{13}C , -7.16 MeV for ^{16}O , and -6.23 MeV for ^{18}O) reveal a larger F_{ICF} for ^{18}O decreasing for ^{16}O , ^{12}C , and ^{13}C , indicating lower negative Q_α values correlate with larger F_{ICF} and vice-versa. The data reveal that for the same targets, the F_{ICF} is higher for ^{12}C compared to ^{13}C projectile. This suggests that a more negative Q_α value enhances projectile break-up, thereby facilitating the onset of ICF. Furthermore, the results highlight a strong dependence of ICF on projectile structure, distinguishing between α -clustered and non- α -clustered projectiles interacting with the same target. These findings underscore the significance of Q_α as a key entrance-channel parameter, providing a deeper understanding of the projectile structure impact on ICF dynamics.

D. Universal Fusion Function: The case of $^{12}\text{C}+^{193}\text{Ir}$ system

The experimental fusion cross-sections (σ_F) have been transformed into the dimensionless function $F(x)$, and the incident energy into a dimensionless variable x , using a method proposed by Canto et al. [74] as,

$$E_{c.m.} \rightarrow x = \frac{E_{c.m.} - V_b}{\hbar\omega}; \sigma_F \rightarrow F(x) = \frac{2E_{c.m.}}{\hbar\omega R_b^2} \sigma_F, \quad (2)$$

where $E_{c.m.}$ is the center-of-mass energy, σ_F is the fusion cross-section, and $\hbar\omega$, R_b , and V_b represent the barrier curvature, barrier radius, and barrier height, respectively. The values of barrier parameters, $\hbar\omega = 4.590$ MeV, $R_b = 11.313$ fm, and $V_b = 55.709$ MeV are sourced from the NRV code [75]. This method is inspired by Wong's formula for fusion cross-section [76],

$$\sigma_F^W(E_{c.m.}) = \frac{R_b^2 \hbar\omega}{2E_{c.m.}} \ln \left[1 + \exp \left(\frac{2\pi(E_{c.m.} - V_b)}{\hbar\omega} \right) \right]. \quad (3)$$

The Universal Fusion Function (UFF), $F_0(x) = \ln[1 + \exp(2\pi x)]$, is constant across different systems. Any deviation from the UFF may be attributed to the effects of projectile break-up on CF cross-sections [77]. The UFF for the $^{12}\text{C}+^{193}\text{Ir}$ system is shown in Fig. 13, with the dotted line representing the UFF multiplied by the suppression factor, $F_{BU} = \frac{F(x)}{F_0(x)}$. The value of F_{BU} is 0.88 times the UFF, determined by fitting the experimental fusion function data in Fig. 13.

Wang's empirical formula may be used to correlate the suppression with break-up threshold energy ($E_{B.U.}$) [77],

$$\log_{10}(1 - F_{B.U.}) = -a \exp \left(\frac{-b}{E_{B.U.}} \right) - c E_{B.U.}, \quad (4)$$

where a , b , and c are the fitting parameters, and their values by Wang et al. are 0.33, 0.29 MeV, and 0.087

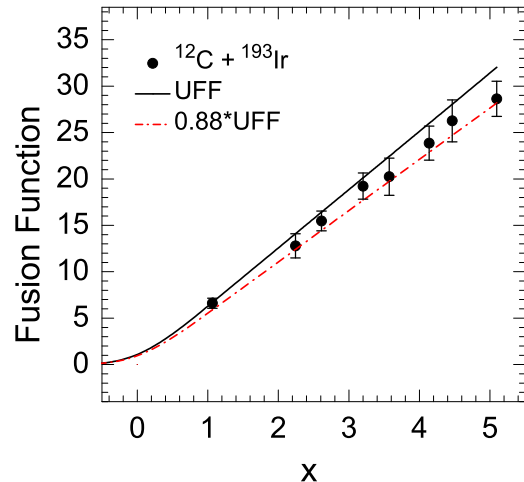


FIG. 13. The fusion function for $^{12}\text{C}+^{193}\text{Ir}$ system indicating a suppression of $\approx 12\%$ in CF compared to UFF.

TABLE V. The value of $F_{B.U.}$ for various projectiles from Wang formulation [77] and modified Eq. 6.

Projectile	$E_{B.U.}$ (MeV)	Wang's equation	Modified (Eq. 6)	$F_{B.U.}$	\log_{10} ($1 - F_{B.U.}$)
^6Li	1.473	-0.40	-0.34	0.60	-0.40
^7Li	2.467	-0.51	-0.45	0.66	-0.47
^{12}C	7.367	-0.96	-0.89	0.88	-0.92
^{13}C	10.648	-1.25	-1.18	0.93	-1.15
^{14}N	11.62	-1.33	-1.26	0.945	-1.26
^{16}O	7.161	-0.94	-0.87	0.85	-0.82
^{19}F	4.014	-0.66	-0.60	0.74	-0.59

MeV $^{-1}$. Eq. 4 becomes,

$$\log_{10}(1 - F_{B.U.}) = -0.33 \exp \left(\frac{-0.29}{E_{B.U.}} \right) - 0.087 E_{B.U.} \quad (5)$$

In Fig. 14, the variation of F_{BU} for different projectiles is plotted as a function of their E_{BU} . The dotted line represents the suppression trend according to Eq. 5. However, the experimental data do not agree with this. Therefore, the constants (i.e., a , b , and c) in Eq. 4 have been adjusted to 0.28, 0.39 MeV, and 0.085 MeV $^{-1}$,

$$\log_{10}(1 - F_{B.U.}) = -0.28 \exp \left(\frac{-0.39}{E_{B.U.}} \right) - 0.085 E_{B.U.} \quad (6)$$

As can be seen in Fig. 14, after implementing the adjusted constants, the experimental data for different projectiles agree reasonably well with that estimated using Eq. 6, unlike Eq. 5. Further, the $\log_{10}(1 - F_{BU})$ values from Eq. 6, fitted to the experimental data for various systems, are listed in Table V. This relationship indicates that E_{BU} affects projectile break-up and, thus, the fusion cross-section.

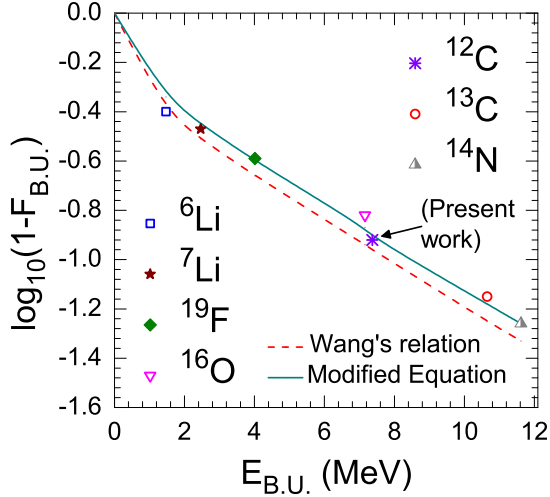


FIG. 14. The $F_{B.U.}$ for different projectiles with their $E_{B.U.}$. The dotted line corresponds to Wang's Eq. 5, while the solid line represents Eq. 6.

V. SUMMARY AND CONCLUSION

In this work, channel-by-channel EFs of different ERs have been measured in $^{12}\text{C}+^{193}\text{Ir}$ system at $\approx 5\text{--}7$ MeV/nucleon and analyzed in the framework of theoretical model code PACE4. The EFs of xn and pxn channels have been well reproduced by PACE4 calculations with input level density parameter $a = A/13 \text{ MeV}^{-1}$, indicating the population of these residues by CF. However, the pxn channels are populated via precursor decay through their higher charge isobars. To supplement the accuracy of xn and pxn channel cross-sections, the value of the Coulomb barrier (V_b) of $^{12}\text{C}+^{193}\text{Ir}$ system has been

deduced from the CF cross-sections which are in good agreement with theoretical values, confirming the accuracy of the measurements. Additionally, the EFs of α -emitting channels display significant enhancement over PACE4 calculations, indicating the onset of ICF.

For a better insight into the onset and influence of ICF, the percentage fraction of ICF (F_{ICF}) has been analyzed in the framework of entrance-channel mass-asymmetry and the Coulomb effect. It has been found that the probability of ICF increases with beam energy, indicating its sensitivity to the projectile energy. The F_{ICF} value in light with μ_m shows a strong dependence on the projectile type. Low-energy ICF data for different systems, with $Z_P Z_T$ (294–568), indicate that break-up probability depends on both projectile structure and Q_α value. To analyze ICF data, no single parameter thoroughly explains ICF dynamics; projectile structure, Q_α , and entrance-channel parameters must be considered. Further, the fusion function derived from CF cross-sections is found to be $\approx 12\%$ lower than the universal fusion function, attributed to prompt projectile break-up. Moreover, Wang's empirical relation [77] leads to confirmation that the projectile break-up is influenced by its break-up threshold energy.

ACKNOWLEDGMENTS

The authors acknowledge the Inter-University Accelerator Centre (IUAC), New Delhi, for facilities to carry out this experiment. One of the authors, Amanjot, thanks the Department of Science & Technology (DST), Govt. of India, for the INSPIRE Doctoral Fellowship (DST/INSPIRE Fellowship/2019/IF190067), and MKS thanks to the SERB-DST for the SURE Grant vide ref.SUR/2022/03462.

-
- [1] R. Broda, J. Phys. G: Nucl. Part. Phys. **32**, R151 (2006).
[2] D. Rudolph *et al.*, Phys. Rev. Lett. **111**, 112502 (2013).
[3] R. Van den Bossche *et al.*, Phys. Rev. C **102**, 064618 (2020).
[4] M. Mougeot *et al.*, Nature Physics **17**, 1099 (2021).
[5] C. E. Düllmann *et al.*, Radiochim. Acta **110**, 417 (2022).
[6] R. Schneider *et al.*, Z. Phys. A - Hadrons and Nuclei **348**, 241 (1994).
[7] J. Pochodzalla *et al.*, Phys. Lett. B **181**, 33 (1986).
[8] H. Wilschut *et al.*, Phys. Lett. B **138**, 43 (1984).
[9] K. Siwek-Wilczyńska *et al.*, Phys. Rev. Lett. **42**, 1599 (1979); Nucl. Phys. A **330**, 150 (1979).
[10] J. Wilczyński *et al.*, Phys. Rev. Lett. **45**, 606 (1980); Nucl. Phys. A **216**, 386 (1973).
[11] H. C. Britt and A. R. Quinon, Phys. Rev. **124**, 877 (1961).
[12] J. Galin *et al.*, Phys. Rev. C **9**, 1126 (1974).
[13] D. Zolnowski *et al.*, Phys. Rev. Lett. **41**, 92 (1978).
[14] C. Gerschel, Nucl. Phys. A **387**, 297 (1982).
[15] J. Beene *et al.*, Phys. Rev. C **23**, 2463 (1981).
[16] J. Barker *et al.*, Phys. Rev. Lett. **45**, 424 (1980).
[17] B. B. Kumar *et al.*, Phys. Rev. C **59**, 2923 (1999).
[18] E. Buthelezi *et al.*, Nucl. Phys. A **734**, 553 (2004).
[19] S. Mukherjee *et al.*, Int. J. Mod. Phys. E **15**, 237 (2006).
[20] M. K. Sharma *et al.*, J. Phys. Soc. Jpn. **72**, 1917 (2003).
[21] A. K. Jashwal *et al.*, Eur. Phys. J. Plus **138**, 1 (2023).
[22] S. A. Tali *et al.*, Phys. Rev. C **100**, 024622 (2019); Nucl. Phys. A **970**, 208 (2018).
[23] A. Ojha *et al.*, India J. Pure Appl. Phys. **58**, 376 (2022); Phys. Rev. C **104**, 034615 (2021).
[24] R. N. Sahoo *et al.*, Nucl. Phys. A **983**, 145 (2019).
[25] S. Chakrabarty *et al.*, Nucl. Phys. A **678**, 355 (2000).
[26] H. Kumar *et al.*, Eur. Phys. J. A **54**, 1 (2018); Nucl. Phys. A **960**, 53 (2017); Phys. Rev. C **99**, 034610 (2019).
[27] K. S. Babu *et al.*, Nucl. Phys. A **739**, 229 (2004).
[28] P. Kaur *et al.*, Phys. Rev. C **105**, 014629 (2022); Eur. Phys. J. Plus **137**, 1287 (2022).
[29] P. Vergani *et al.*, Phys. Rev. C **48**, 1815 (1993).
[30] K. Kalita, J. Phys. G: Nucl. Part. Phys. **38**, 095104 (2011).

- [31] A. S. Valdés *et al.*, Phys. Lett. B **843**, 138026 (2023).
- [32] T. Udagawa *et al.*, Phys. Rev. Lett. **45**, 1311 (1980).
- [33] J. P. Bondorf *et al.*, Nucl. Phys. A **333**, 285 (1980).
- [34] H. Morgenstern *et al.*, Phys. Rev. Lett. **52**, 1104 (1984), and references therein.
- [35] P. P. Singh *et al.*, Phys. Rev. C **77**, 014607 (2008).
- [36] K. Kumar *et al.*, Phys. Rev. C **89**, 054614 (2014).
- [37] V. R. Sharma *et al.*, Phys. Rev. C **89**, 024608 (2014).
- [38] A. Yadav *et al.*, Phys. Rev. C **96**, 044614 (2017); in *EPJ Web of Conferences*, Vol. 96 (EDP Sciences, 2015) p. 01035.
- [39] A. Agarwal *et al.*, Phys. Rev. C **105**, 034609 (2022); **103**, 034602 (2021); Phys. of Part. and Nuclei **54**, 677 (2023).
- [40] R. Rafiei *et al.*, Phys. Rev. C **81**, 024601 (2010).
- [41] D. Hinde *et al.*, Phys. Rev. Lett. **89**, 272701 (2002).
- [42] P. Gomes *et al.*, Phys. Lett. B **601**, 20 (2004).
- [43] M. Shuaib *et al.*, Phys. Rev. C **94**, 014613 (2016).
- [44] D. Singh *et al.*, Phys. Rev. C **97**, 064604 (2018).
- [45] M. Kumar *et al.*, Phys. Rev. C **100**, 034616 (2019).
- [46] M. Kumar *et al.*, Eur. Phys. J. Plus **139**, 1 (2024).
- [47] P. K. Giri *et al.*, Phys. Rev. C **100**, 024621 (2019).
- [48] D. Singh *et al.*, Phys. Rev. C **97**, 064610 (2018).
- [49] A. Nasirov *et al.*, Phys. Lett. B **842**, 137976 (2023).
- [50] P. Eudes *et al.*, Phys. Rev. C **90**, 034609 (2014).
- [51] A. Yadav *et al.*, Phys. Rev. C **107**, 044605 (2023).
- [52] W. Xu *et al.*, Phys. Lett. B **839**, 137789 (2023).
- [53] I. Lee *et al.*, J. Phys. G: Nucl. Part. Phys. **47**, 015101 (2019).
- [54] P. P. Singh *et al.*, Phys. Lett. B **671**, 20 (2009); Phys. Rev. C **80**, 064603 (2009).
- [55] Amanjot *et al.*, Vacuum **226**, 113287 (2024).
- [56] SRIM, <http://www.srim.org/>.
- [57] E. Subramaniam *et al.*, Rev. Sci. Instr. **77** (2006).
- [58] CANDLE, <http://www.iuac.res.in/NIAS/?url=Downloads/>.
- [59] NNDC, <http://www.nndc.bnl.gov>.
- [60] M. Kaushik *et al.*, Phys. Rev. C **101**, 034611 (2020).
- [61] E. Browne and R. B. Firestone, *Table of Radioactive Isotopes* (Wiley, New York, 1996).
- [62] J. K. Tuli *et al.*, *Nuclear wallet cards* (Brookhaven National Laboratory Upton, 1995).
- [63] A. Gavron, Phys. Rev. C **21**, 230 (1980); LISE++, <https://lise.nsc1.msu.edu/lise.html>.
- [64] M. K. Sharma *et al.*, Phys. Rev. C **94**, 044617 (2016), and references therein.
- [65] M. Cavinato *et al.*, Phys. Rev. C **52**, 2577 (1995).
- [66] A. Yadav *et al.*, Phys. Rev. C **85**, 034614 (2012).
- [67] S. Gupta *et al.*, Phys. Rev. C **61**, 064613 (2000).
- [68] D. Singh *et al.*, Phys. Lett. B **774**, 7 (2017).
- [69] K. Kumar *et al.*, Phys. Rev. C **88**, 064613 (2013).
- [70] M. K. Sharma *et al.*, Nucl. Phys. A **776**, 83 (2006).
- [71] K. Kumar *et al.*, Phys. Rev. C **87**, 044608 (2013).
- [72] H. Kumar, *Ph.D. thesis* (Aligarh Muslim University, 2017).
- [73] A. Yadav *et al.*, in *EPJ web of conferences*, Vol. 117 (EDP Sciences, 2016) p. 08022.
- [74] L. F. Canto *et al.*, Nucl. Phys. A **821**, 51 (2009), and references therein.
- [75] NRV, <http://nrv.jinr.ru/nrv/webnrv/fusion/>.
- [76] C. Wong, Phys. Rev. Lett. **31**, 766 (1973).
- [77] B. Wang *et al.*, Phys. Rev. C **90**, 034612 (2014).